NANO LETTERS
Letter
Cite This: Nano Lett. 2019, 19, 8503−8509
pubs.acs.org/NanoLett

Mod(n-m,3) Dependence of Defect-State Emission Bands in Aryl-Functionalized Carbon Nanotubes

Brendan J. Gifford,[†,‡,§] Avishek Saha,[‡,▽] Braden M. Weight,[§,○] Xiaowei He,[‡] Geyou Ao,[⊥] Ming Zheng,[⊥] Han Htoon,[‡] Svetlana Kilina,[∥] Stephen K. Doorn,*[,‡] and Sergei Tretiak*[,†,‡,§]

[†]Center for Nonlinear Studies, [‡]Center for Integrated Nanotechnologies, Materials Physics and Applications Division, and [§]Theoretical Division, Los Alamos National Laboratory, Los Alamos, New Mexico 87545, United States

[∥]Department of Chemistry and Biochemistry and [○]Department of Physics, North Dakota State University, Fargo, North Dakota 58108, United States

[⊥]Materials Science and Engineering Division, National Institute of Standards and Technology, Gaithersburg, Maryland 20899-8540, United States

[▽]CSIR-Central Scientific Instruments Organization, Chandigarh 160030, India

Supporting Information

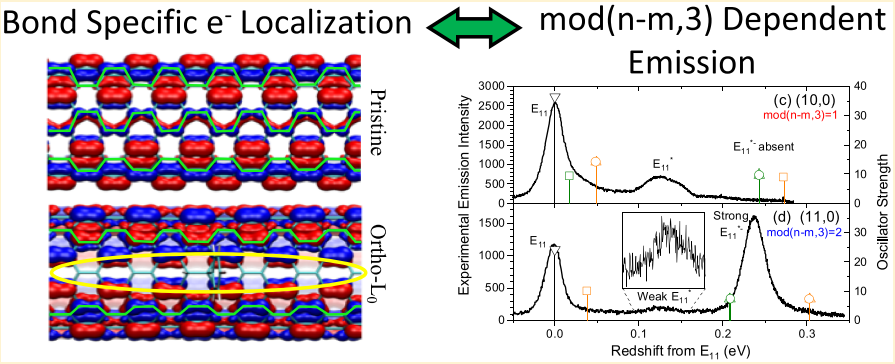

ABSTRACT: Molecularly functionalized single-walled carbon nanotubes (SWCNTs) are potentially useful for fiber optical applications due to their room temperature single-photon emission capacity at telecommunication wavelengths. Several distinct defect geometries are generated upon covalent functionalization. While it has been shown that the defect geometry controls electron localization around the defect site, thereby changing the electronic structure and generating new optically bright red-shifted emission bands, the reasons for such localization remain unexplained. Our joint experimental and computational studies of functionalized SWCNTs with various chiralities show that the value of mod(n-m,3) in an (n,m) chiral nanotube plays a key role in the relative ordering of defect-dependent emission energies. This dependence is linked to the complex nodal characteristics of electronic wave function extending along specific bonds in the tube, which justifies the defect-geometry dependent exciton localization. This insight helps to uncover the essential structural motifs allowing tuning the redshifts of emission energies in functionalized SWCNTs.

KEYWORDS: *carbon nanotubes, nanomaterials, photonic materials, organic color centers, fiber optics*

Single-walled carbon nanotubes (SWCNTs) are pseudo one-dimensional structures constructed by rolling a graphene sheet into a cylinder.[1,2] The direction in which the sheet is rolled is described by a chiral vector constructed from two vectors **n** and **m** lying at +30° and −30° from the armchair dimension of the graphene sheet.[3] This construction allows for the generation of distinct tube geometries (n,m), known as "chiralities", with unique electronic[4] and optical properties.[5] The experimentally observed dependence of optical band energies of SWCNTs on their precise chiral structure follows the "family behavior"—a systematic pattern of chirality dependence of the optical transition energies in semiconducting SWCNTs according to whether mod(n-m, 3) = 1 (denoted as mod1) or 2 (dubbed as mod2).[6] When mod(n-m,3) = 0, the tubes are metallic and will not be considered for this study. In addition to chirality dependence, the emission energies of pristine SWCNTs follow the diameter-dependent trends predicted by quantum confinement (i.e., particle in a box), where larger diameter tubes generate lower-energy emission features.[7] Such energy dependence allows for the precise spectroscopic characterization of chiralities present in a sample and offers a great deal of tunability for applications requiring

Received: July 17, 2019
Revised: September 25, 2019
Published: November 4, 2019

DOI: 10.1021/acs.nanolett.9b02926
Nano Lett. 2019, 19, 8503−8509

different energies of optical features.[8] For fiber-optical applications, room-temperature single-photon emission in the infrared range is desired.[9] While near-infrared emission can be achieved from relatively large pristine SWCNTs, quantum yields of emission are typically low due to the presence of low-lying dark states at energies lower than the bright optical transition. Furthermore, the excitons rapidly diffuse and quench at defects formed in the tube synthesis.[10] Covalent functionalization of SWCNTs presents a new strategy for manipulating their optical properties and brightening the lowest-energy optical transition. Chemical adducts on the surface create localized low-lying excited states able to trap diffusing excitons, thereby increasing emission quantum yields and red shifting the emission features, thus accessing telecom wavelengths from the relatively small diameter SWCNTs that are generated from common synthetic methods.[10−14]

A common functionalization process involves chemically treating SWCNTs with aryl diazonium reagents,[15−20] resulting in sparse integration of low-level sp^3-defects in the otherwise sp^2-hybridized lattice. The first step in this functionalization process involves a charge transfer between the SWCNT and the reactive aryl species resulting in a reactive intermediate. Resonance relocates charge (or an unpaired electron in the case of a radical mechanism) to positions either *ortho* or *para* with respect to the original addition site in configurations along the three types of chemically distinct bonds present in SWCNTs.[11] These three types of bonds are labeled (+), (++), and (−) as shown in Figure 1a,b. Carbon atoms along each of these three types of bonds become candidates for addition of a second species (being another aryl group or an H or OH from aqueous media).[21] It has recently been demonstrated that such additions result in distinct defect geometries exhibiting different emission energies.[21] In the absence of functionalization, the emission spectra of a single chirality SWCNT contains a single well-defined feature at energy E_{11}. Depending on the functionalization conditions, one or two defect-based emission bands generally emerge: one with redshifts of ∼100 meV from the native exciton (denoted by E_{11}^*) and one with redshifts of ∼200 meV (denoted by E_{11}^{*-}). These emission features originate from defects of different geometries, and the generation of multiple defect geometries accounts for the presence of emission features over a wide range of energies.[21] The energies of the emission features for different functionalization configurations with respect to the SWCNT axis also exhibit significant chirality dependence.[22,23] It has been further demonstrated through a number of spectroscopic studies that ortho-functionalized configurations (Figure 1a) are likely the predominant species formed in the reaction due to differences in reactivity toward specific defect geometries.[23] This varying reactivity is attributed to π-orbital mismatch in pristine SWCNTs, where bonds directed along the axis of the tube are not as reactive as others due to increased π-orbital overlap. Zigzag SWCNTs (chiral angle = 0°) have been shown to exhibit reduced spectral diversity compared to other chiralities due to the symmetry in the SWCNT lattice creating two degenerate defect geometries.[22,23] While strong redshifts in emission features of certain defect geometries have been correlated to exciton localization,[10,11,14] a rationale behind such localization is currently lacking. In order to attain tighter control of functionalized SWCNT emission features, further insights into the source of geometry-dependent localization are required.

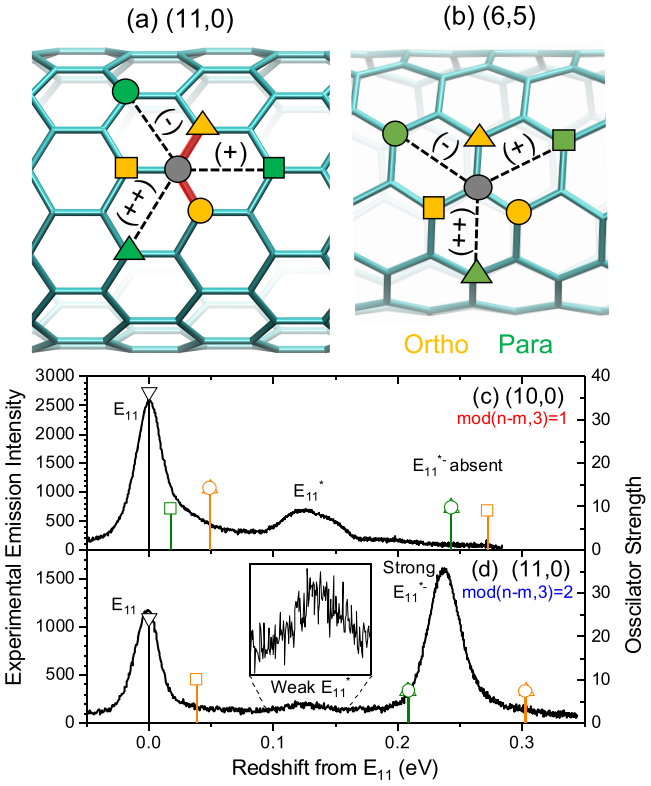

Figure 1. Possible functionalization positions on a (a) zigzag SWCNT and (b) chiral SWCNT. With a functional group added to the initial functionalization site (gray circle), a second group could add to the other six positions to yield (+) (square), (++) (triangle), or (−) (circle) defect geometries. This addition can occur either adjacent to the initial site (to form ortho, yellow) or across the ring from the initial site (to form para, green). The bonds highlighted in red are those that are most reactive. Experimental (black curve) and calculated (stick spectra) emission spectra of functionalized (c) (10,0) and (d) (11,0) SWCNTs (methoxybenzene dopant was used for experimental, and bromobenzene group for computed systems, see Methods). Stick spectra correspond to the calculated transition energies for functionalization in the ortho(+) (squares), ortho(++) (triangles), and ortho(−) (circles) configurations. Orange symbols and droplines indicate the energies of ortho-functionalized species, while green symbols and droplines indicate the energiesof para-functionalized species. Functionalization of (10,0) (a mod1 system) results in the presence of E_{11}^* emission features, while the E_{11}^{*-} peak is absent. Functionalization of (11,0) (a mod2 system) leads to strong E_{11}^{*-} and very weak E_{11}^* features. These results can be understood by considering π-orbital mismatch in the pristine systems as well as degeneracies imposed by the zigzag tube symmetry.

Here, we theoretically model a set of functionalized zigzag SWCNTs of different diameters and mod(n-m,3) families using time-dependent density functional theory (DFT) for computations of emission energies for the finite-length segments and compare these results to available experimental spectra. This approach has been previously shown to produce results consistent with experimental data for a variety of chemical species.[10−14,23] Analysis of the optical features obtained from our calculations suggest a family dependence in mod1 and mod2 zigzag nanotubes for the energies of emission features with respect to defect geometries. This dependence is shown to agree with experimental data. We extend these observations to functionalized SWCNTs of varying chiralities, thereby demonstrating that these mod-

DOI: 10.1021/acs.nanolett.9b02926
Nano Lett. 2019, 19, 8503−8509

dependent trends are not limited to zigzag systems. Such an observation is in agreement with experimental results demonstrating that the energy of E_{11}* transitions follows mod(n-m,3) family based trends.[13,24,25] It further suggests trends in optical shifts that can assist in the assignment of individual spectral features to specific binding configurations for each tube chirality. We further provide physical interpretations for the strong redshifts of optical features. For the first time, we attribute exciton localization at defects to geometry-dependent variation in the nodes of the frontier orbital wave functions extending through the honeycomb tube lattice.

Functionalization of zigzag SWCNT chiralities with different mod(n-m,3) values reveals opposite behavior with respect to intensity of different emission features. For mod1 (10,0) tubes, the predominant emission feature observed is the higher-energy E_{11}*, while peaks at the lower-energy E_{11}*$^{-}$ are completely absent. In contrast, the functionalized mod2 (11,0) spectrum exhibits strong features at E_{11}*$^{-}$ and only very weak emission at E_{11}* (Figure 1c,d). Chiral angle and tube diameter cannot be the source of this discrepancy since both have the same chiral angle (0°) and similar diameters (0.78 nm for (10,0) and 0.86 nm for (11,0)). Furthermore, different defect geometries cannot account for observed difference since it is expected that functionalization of any zigzag system will result in the formation of similar off-axial defect geometries due to the reactivities of these bonds. Previous results have attributed the increased reactivity of certain bonds due to high π-orbital misalignment, which in turn was linked to increased selectivity for functionalization along bonds lying away from either the SWCNT axis or circumference.[23] Namely, the less-reactive bonds along the nanotube axis have minimal misalignment compared to the reactive bonds oriented farther away from the axis, which are distorted by the tube curvature. However, in the present case, both (10,0) and (11,0) SWCNTs are of zigzag chirality. There are therefore only minor differences in π-orbital misalignment of corresponding bonds for both SWCNTs, as supported by our calculations (Figure S2). Stronger misalignment for both reactive and nonreactive types of bonds are observed for smaller nanotubes than for larger ones due to their increased curvature. However, the overall reactivity trends are consistent across all chiralities. It is therefore expected that the same types of bonds would react in both mod1 and mod2 zigzag SWCNTs producing similar topological defect geometries. Thus, the observed differences in the experimental emission features of (10,0) and (11,0) SWCNTs (Figure 1c,d) are surprising and cannot be explained by existing understanding.

With this in mind, we invoke quantum chemical modeling to rationalize the differences in the two spectra. As with previous reports, the defect geometry strongly influences the energies of optical features. While relative bond reactivity dictates that ortho functionalization is more preferential, some experimental emission features best correlate to the energies predicted by para structures.[22] We therefore study the effects of both ortho and para functionalization along three types of bonds distinct in the angle they form with respect to the SWCNT axis (Figure 1a). Symmetry in zigzag SWCNTs leads to a degeneracy of (−) and (++) bonds oriented away from the SWCNT axis and results in a single emission feature for functionalization along these two bonds (stick spectrum, Figure 1c,d). For functionalized (11,0), this configuration corresponds to a strongly redshifted E_{11}*$^{-}$ feature, consistent with pronounced experimental spectral feature (Figure 1d). The strength of this feature indicates that it likely is the result of the defect along the highly reactive off-axial bonds. Additionally, functionalization along the less-reactive axial ortho (+) bond and para functionalization occurs only to a small degree, leading to a very weak less red-shifted E_{11}* feature (Figure 1d).[23] Analysis of a functionalized (10,0) tube demonstrates opposite trends. In a stark contrast to (11,0), functionalization in the degenerate orientations along ortho(−) and ortho(++) bonds leads to much smaller redshifts (Figure 1c). Thus, an E_{11}* feature present in the experimental spectrum is likely the result of either ortho or para functionalization in such orientations. Moreover, axial functionalization of (10,0) to form the ortho (+) configuration would result in formation of the more strongly red-shifted emission feature. This peak is absent from the experimental spectrum. Since the smaller diameter of (10,0) results in greater π-orbital misalignment across all bonds (Figure S2), the selectivity toward functionalization of nonaxial bonds is stronger than that for (11,0). As such, axial functionalization does not occur and E_{11}*$^{-}$ features are completely absent from the experimental spectrum for the (10,0) system (Figure 1c). A mod(n-m,3) dependence in spectral energies is suggested by these differences in experimental and calculated optical spectra for (10,0) and (11,0) systems.

To confirm and generalize the mod-dependent effects on optical transition energies in a wider range of tube chiralities, we have calculated the energies of optical features for ground-state geometries for a set of functionalized SWCNTs spanning a wide range of diameters and chiral angles (Figure 2). Analysis of optical features calculated from ground-state geometries is sufficient to establish trends in optical energies with respect to defect configuration since the redshifts from E_{11} for absorption and emission features have been shown to be qualitatively similar.[14] Figure 2 demonstrates that mod-dependent optical energies are not limited to zigzag systems: a distinct mod-dependent behavior is observed across all chiralities. When the functionalized bond is close to the axis (as is the case for ortho(+) functionalization), the redshift for mod1 is the strongest among the different defect geometries (Figure 2, red circles). In contrast, defect configurations from functionalization close to the axis for mod2 systems generate the smallest redshift among all species of ortho(+). Furthermore, mod2 systems generate the strongest redshifts for defect configurations forming a negative angle with respect to the SWCNT axis (ortho(−) systems), Figure 2, blue circles. Similar negative angles for mod1 systems lead to very small redshifts from E_{11}. In all cases, functionalization of the bond closest to the SWCNT circumference (ortho(++)) results in some intermediate energy shifts between the other two configurations, with the exception of zigzag systems where two degenerate defect geometries exist. It is notable that the degree of redshift when going across the series varies dependent on the diameter of the SWCNT. Generally, the larger tubes exhibit the smaller total redshifts. This behavior has been previously described for E_{11}* features.[13,25,26] Our current computational results suggest a similar trend for E_{11}*$^{-}$ features originating from different defect configurations. We note that the observed trends are opposite for para configurations, which also show the distinct mod and diameter dependence (bottom three panels of Figure S3). However, functionalization in para positions is expected to generate the least synthetically relevant defects, due to the less reactive nature of these configurations.[23] While the mod-

DOI: 10.1021/acs.nanolett.9b02926
Nano Lett. 2019, 19, 8503−8509

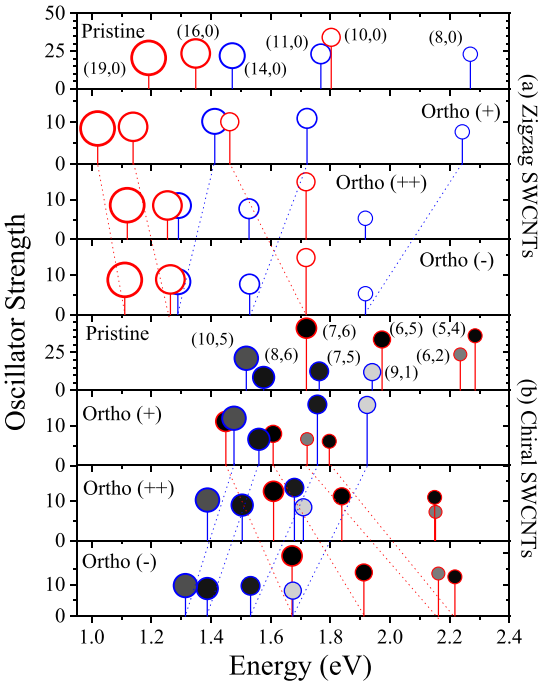

Figure 2. Chirality dependence of optical features for aryl-functionalized (a) zigzag SWCNTs and (b) chiral SWCNTs. All energies correspond to vertical transitions in the ground-state optimal geometries. Red and blue points represent chiralities where mod(n-m,3) = 1 or 2, respectively. The size of the data points is indicative of the diameter of the SWCNT. The density of fill corresponds to the chiral angle, where open points are zigzag systems ($\theta = 0°$) while fully filled points correspond to near-armchair systems ($\theta \approx 30°$). Dashed lines connect the least and most red-shifted functionalization configurations for each species, demonstrating a higher range of redshifts for smaller diameter tubes compared to larger ones. The degree of redshift for functionalization angles near versus far from the SWCNT axis is highly dependent on mod(n-m,3) values. Transition energies are clearly dependent on SWCNT diameter, where larger tubes have lower transition energies. The chiral angle appears to play a little role in dictating the transition energies.

dependent and diameter-dependent trends in optical features for different defect geometries have previously attributed to differences in the degree of exciton localization,[14] the physical origins for such localization are yet to be explained. Comparison of the frontier molecular orbitals of a mod1 and mod2 system rationalizes these observations.

A general trend for emission features as exemplified for functionalized (6,5) SWCNTs is that the introduction of sp^3-defects in different configurations results in varying redshifts from E_{11} due to exciton localization around the defect site. Here the most localized species generate the strongest redshifts compared to less-localized configurations.[14,21] The same remarks apply to the zigzag systems explored here. Strong defect-induced wave function localization is observed for the ortho(+) configuration for (10,0) (Figure S4) or degenerate ortho(++) and ortho(−) configurations for (11,0) (Figure S5). This localization is concomitant to destabilization of the highest-occupied molecular orbital (HOMO) and stabilization of the lowest-unoccupied molecular orbital (LUMO), resulting in a drastically reduced HOMO−LUMO gap (Figure S6). Since the predominant optically active transition in functionalized SWCNTs involves a $\pi \rightarrow \pi^*$ transition between the HOMO and LUMO (Table S1), these perturbations to the electronic structure results in a significantly reduced many-electron band gap and thus red-shifted emission features. The wave function localization in the frontier molecular orbitals reflects the localization in the exciton for the same reason.

The origin of wave function localization can be explained by examining the nature of the HOMO and LUMO orbital nodes. For pristine mod2 systems, the electron distribution in the HOMO is spread across (+) bonds (Figure 3a) with π-electron

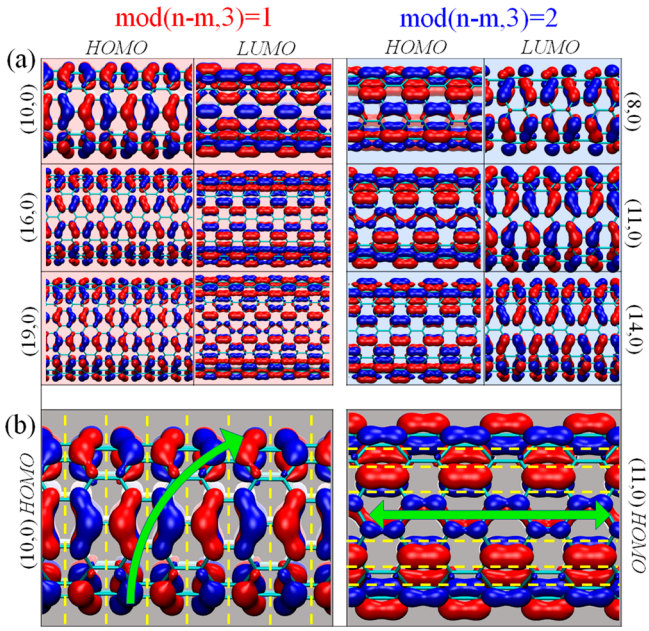

Figure 3. (a) Electron density of the HOMO and LUMO for pristine mod1 (red background) and mod2 SWCNTs (blue background), and (b) nodal structure in the HOMO for a pristine mod1 ((10,0), left) and mod2 SWCNT ((11,0), right). Yellow dashes indicate the position of the nodes, and the green arrows represent the extent of the region of orbitals with constructive phase overlap. All systems are oriented such that the tube axis runs horizontally.

orbitals of the same phase being oriented parallel to the SWCNT axis (Figure 3b). Thus, long node-free paths (denoted by green arrow) are parallel to the tube axis (Figure 3b, Figure S7). When functionalization is performed along an (+) bond in the mod2 (11,0) system, the resulting bond lies parallel to the nodes and perturbations to the electronic structure are minimal, Figure 4. The electron distribution now avoids the bonds lacking π density (i.e., sp^3-hybridized carbon atoms) and takes an advantage of the adjacent node-free paths remaining along the SWCNT axis. As a result, the ability of the functionalized system to delocalize π -orbitals is similar to that of the pristine system and the electronic structure and optical properties of the system functionalized along (+) only marginally deviates from the pristine case. However, this holds only for (+) functionalization: the nodes are bisected by the defect when the mod2 system has a pair of sp^3-carbons along either (++) or (−) bonds. This results in a significant disturbance to the nodal structure in the vicinity of the defect, where out-of-phase electronic structure is introduced onto the carbon atom adjacent to the functionalized one (highlighted by yellow circle in Figure 4). This disrupts the long node-free path, and electron delocalization is hindered, Figure 4. The resulting functionalized system thus opts for localized orbitals compared to the pristine system. That interrupted or perpetual

DOI: 10.1021/acs.nanolett.9b02926
Nano Lett. 2019, 19, 8503−8509

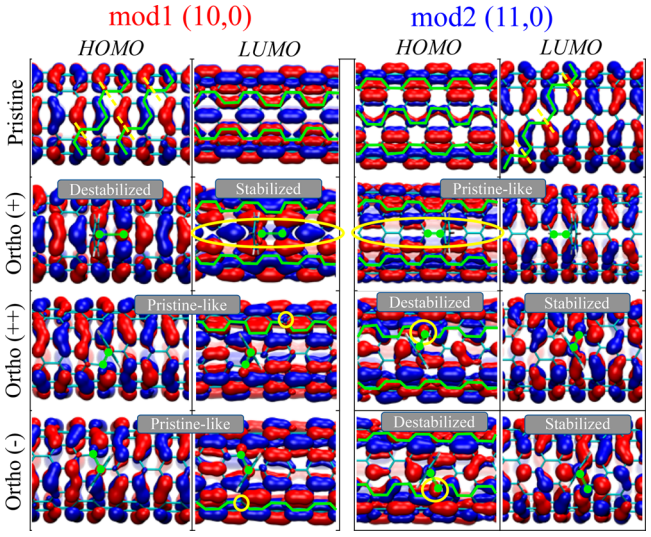

Figure 4. Electron density of the HOMO and LUMO for functionalized mod1 (red background) and mod2 SWCNTs (blue background). Green traces indicate regions of continuous electron delocalization due to same orbital phase overlap. Yellow dashed lines indicate where a node disrupts electron delocalization. Green dots connected by a line indicate the carbon atoms that are functionalized and the bond that is converted to a single bond upon functionalization. The yellow ovals highlight the large regions of loss of electron density in that MO due to functionalization. The HOMO in the mod1 system contains nodes parallel to the SWCNT axis, allowing for electron delocalization in the axial direction. Functionalization along ortho(+) preserves this electronic structure everywhere except on a line through the defect. Functionalization along ortho(++) or ortho(−), however, introduces a node into the electronic structure along the remaining lines. Electron delocalization near the defect site is thereby interrupted, leading to appearance of spatially localized orbitals near the defect site.

electronic communication is the source of destabilization of the HOMO, stabilization of the LUMO, the reduced HOMO−LUMO gap, and the red-shifted emission features for mod2 systems functionalized in specific orientations (e.g., (++) or (−) for zigzag case).

Unlike in the mod2 systems, the HOMO of mod1 SWCNTs exhibits in-phase electron distribution along the (++) and (−) bonds. The longest, node-free paths can be found 60° from the SWCNT axis (Figure S7). In this case, the LUMO of mod 1 tubes resembles the HOMO of the mod2 system. Functionalization in the ortho(+) configuration generates an electron distribution somewhat similar to that of the pristine system (Figure 4). However, the bonds on a path that passes directly through both sp^3-hybridized carbon atoms now contain significant electron density (in contrast to the HOMO for ortho(+) of (11,0), where these bonds were avoided). This electron density is localized across the defect state and thereby strongly stabilizes the LUMO (Figure 4), resulting in the significantly red-shifted emission transition. However, similar to the (11,0) case, ortho(+) of (10,0) is expected to be the least reactive configuration due to π-orbital misalignment angles (as discussed before). Therefore, the most red-shifted emission band (E_{11}^{*-}) is expected to be suppressed in the emission spectra of (10,0) SWCNT (see Figure 1a). In contrast, the HOMO and LUMO of the mod1 system functionalized along either the (++) or (−) bonds show much more similar node distribution to those of the HOMO and LUMO of pristine (10,0), with only small perturbations on the defect sites. As a result, functionalizations along (++) or (−) bonds of mod1 SWCNTs show the smallest redshifts of their emission energies with respect to the E_{11} band of pristine SWCNTs (Figure S6). However, comparing to the least red-shifted emission band in the ortho(+) structure of mod2, the larger distortion in orbital localization of the least red-shifted and degenerate features of ortho(++) and ortho(−) structures of (10,0) results in a more red-shifted and optically brighter peak (i.e., E_{11}^* band well pronounced in the experimental spectra, Figure 1) than those of (11,0) SWCNTs (i.e., weak E_{11}^* band, Figure 1). Thus, these qualitative arguments outline the basis for correlating the nodal structure of molecular orbitals in pristine SWCNTs to defect-configuration-dependent differences in electron density and provide an explanation to the mod-dependent optical behavior observed in functionalized SWCNTs.

In conclusion, we have demonstrated that differences in the emission spectra of functionalized (10,0) versus (11,0) SWCNTs are the result of selectivity toward specific degenerate defect geometries that have distinct emission energies falling in the E_{11}^* and E_{11}^{*-} spectral energy ranges, respectively. For the former system, binding configurations generating weakly red-shifted E_{11}^* are exclusively formed, whereas the latter contains a weak E_{11}^* signature along with much stronger E_{11}^{*-}. Due to similarities in π-orbital misalignment angles for both systems, the most reactive functionalization configurations are those that lie away from the tube axis. To justify the presence of E_{11}^* for (10,0) and E_{11}^{*-} for (11,0), it must be concluded that two nonaxial defect geometries produce degenerate emission energies that are highly dependent on tube chirality indices. Quantum chemical simulations validate these findings. Furthermore, analysis of the theoretical emission features of a wider range of zigzag tubes demonstrates a distinct dependence of optical energies on mod(n-m,3) values. Where mod(n-m,3) = 1, the reactive nonaxial configurations result in the formation of degenerate least red-shifted E_{11}^* emission features. The less-reactive axial configurations would produce the strongly red-shifted E_{11}^{*-} features if defects in this configuration were formed, which is only expected to be energetically favorable for zigzag systems larger than (11,0). The opposite trends—where the most red-shifted E_{11}^{*-} features originated from two degenerate reactive nonaxial configurations—are expected for zigzag chiralities where mod(n-m,3) = 2. This strong mod-dependence is not limited to zigzag systems as computationally observed across a series of 14 chiralities, thus indicating its generality. We have been able to justify the mod-dependent behavior by considering the nodal structure of the frontier molecular orbitals in pristine SWCNTs and qualitatively characterizing how it is affected by sp^3 functionalization at defects. If the bond involved in ortho functionalization bisects a node in the HOMO, the resulting electronic structure acquires new nodes that foster localization of electron density around the defect site. This reduces the bandgap through destabilization and stabilization of the HOMO and LUMO, respectively, and redshifts the emission features. However, if the bond does not bisect a node in the HOMO of the pristine structure, the resulting electronic structure remains unperturbed and resembles that of the pristine system. Subsequently, only marginal shifts in the optical properties are observed. This provides insight into the physical traits that direct electron localization/delocalization around the defect site, which in turn

DOI: 10.1021/acs.nanolett.9b02926
Nano Lett. 2019, 19, 8503−8509

control the corresponding shifts in the optical emission features of functionalized SWCNTs.

Methods. *Experimental Methods.* DNA-wrapped SWCNT samples enriched in (10,0), and (11,0) chiralities were isolated using DNA-based aqueous two-phase separation.[27] Before functionalization, SWCNTs were exchanged into 1 wt % aqueous SDS by centrifugal filtration following previously reported work.[23] This generated very pure samples as verified by PL excitation maps (Figure S8b,d) and PL spectra (Figure S8a,c). For (10, 0) functionalization, 160 μL of SWCNTs (E11 OD, 0.014) were doped with aqueous solution of 2 μL of 0.1 mg/mL of 4-bromobenzenediazonium tetrafluoroborate (Aldrich) and 15 μL of 0.05 mg/mL 4-methoxybenze diazonium solution, respectively. The reaction was subsequently quenched by addition of 22 μL of 10 wt % aqueous DOC solution. Another surfactant exchange into 1 wt % DOC/D_2O was performed using membrane centrifugation before measuring the photoluminescence spectra. Functionalization of (11,0) SWCNTs with 4-methoxybenzene diazonium tetrafluoroborate was performed following our previous work.[23] PL spectra of the functionalized SWCNT demonstrate the introduction of the defect-based E_{11}* features (Figure S9) All the ensemble photoluminescence spectra were measured using a Horiba Nanolog spectrofluorometer with 850 nm, long-pass filter in the collection path. Functionalized (10,0) and (11,0) were excited at 540 and 750 nm, respectively.

Computational Methods. Our simulations use a well established modeling approach based on DFT and TD-DFT techniques applied to long segments of functionalized SWCNTs properly capped on the ends.[14,22,28,29] Namely, SWCNTs of ∼12 nm length were generated with the Visual Molecular Dynamics (VMD) software program.[30] SWCNTs of experimental relevance are on the order of micrometers in length, which are prohibitively expensive for nonperiodic computational models.[31−33] The terminal bonds were then capped to replicate the electronic structure of infinite systems as previously described in detail elsewhere.[28,29] Functionalization was performed producing the six experimentally plausible defect configurations.[14] Both the ground-state and excited-state optimized geometries were obtained for (10,0) and (11,0) using DFT and TD-DFT,[34] respectively, as implemented by the Gaussian09 software package.[35] All other chiralities were optimized for only the ground state since trends of energies for calculated absorption and emission have been shown to be consistent.[14] Ground-state frontier molecular orbital (MO) isosurfaces were visualized with an isovalue of 0.01. The excited-state behavior of each system was further explored using TDDFT.[34,36] All computations were performed using the STO-3G basis set[37] and CAM-B3LYP density functional.[38] This methodology has been shown to properly predict electron localization in functionalized SWCNT systems.[14,22,39] Furthermore, errors in methodology and electron confinement were corrected using a previously described scaling scheme enabling comparison with experiment.[22]

The energies of experimental emission features are only slightly affected by functionalization with different monovalent species, where more electron-withdrawing groups generate slightly stronger redshifts.[40] 4-Bromobenzene-functionalized zigzag SWCNTs were used in the theoretical modeling for this study due to the large computational data set available for these species. While 4-methoxybenzene species are typically used in experimental systems, we have functionalized (10,0) chirality enriched SWCNTs using both 4-bromobenzenediazonium and 4-methoxybenzenediazonium (see Experimental Methods). Both systems are expected to be slightly electron withdrawing, but these effects are shielded from the SWCNT by the benzene ring. As such, the differences in the inductive effect felt at the SWCNT from these two systems are only marginally different. Furthermore, since the optical features originate from excitons spatially localized on the SWCNT surface and not the functional group itself,[11,14] only marginal differences in the emission features would be expected as well. Our spectroscopic results on these systems validate these expectations (Figure S1a). This observation, coupled with our previous results exhibiting species independence for emission energies, corroborates the use of computed results for 4-bromobenzene and experimental results for 4-methoxybenzene functional groups. We have further calculated the optical transition energies for (10,0) and (11,0) SWCNTs functionalized with both 4-methoxybenzene and 4-bromobenzene (Figure S1a,b). The calculated transition energies are indeed consistent, independent of the functionalization species for all defect geometries.

■ ASSOCIATED CONTENT

Supporting Information

The Supporting Information is available free of charge on the ACS Publications website at DOI: 10.1021/acs.nanolett.9b02926.

Experimental and computed emission spectra for (10,0) and (11,0) functionalized with diazonium salts, π-orbital mismatch for the zigzag SWCNT systems, calculated optical emission energies for functionalized zigzag and chiral SWCNTs, frontier molecular orbitals of functionalized (10,0) and (11,0) SWCNTs, molecular orbital energies for functionalized (10,0) and (11,0) SWCNTs, contribution of transitions between the frontier molecular orbitals in the TDDFT calculations of functionalized SWCNTs, absorbance spectra, photoluminescence excitation maps, and PL spectra for (10,0) and (11,0) SWCNTs functionalized with bromobenzene, methoxybenzene, and dichlorobenzene (PDF)

■ AUTHOR INFORMATION

Corresponding Authors

*E-mail: skdoorn@lanl.gov.
*E-mail: serg@lanl.gov.

ORCID

Brendan J. Gifford: 0000-0002-4116-711X
Braden M. Weight: 0000-0002-2441-3569
Xiaowei He: 0000-0002-4982-8250
Geyou Ao: 0000-0002-9932-3971
Ming Zheng: 0000-0002-8058-1348
Han Htoon: 0000-0003-3696-2896
Svetlana Kilina: 0000-0003-1350-2790
Stephen K. Doorn: 0000-0002-9535-2062
Sergei Tretiak: 0000-0001-5547-3647

Notes

The authors declare no competing financial interest.

■ ACKNOWLEDGMENTS

This work was conducted, in part, at the Center for Nonlinear Studies and the Center for Integrated Nanotechnologies, U.S.

DOI: 10.1021/acs.nanolett.9b02926
Nano Lett. 2019, 19, 8503−8509

Department of Energy, Office of Basic Energy Sciences user facilities and supported in part by Los Alamos National Laboratory (LANL) Directed Research and Development Funds. S.K. acknowledges NSF Grant CHE-1413614 for financial support of studies of functionalized carbon nanotubes and the Alfred P. Sloan Research Fellowship BR2014-073 for partial support of studies of surface effects at interfaces of nanostructures. For computational resources and administrative support, S.K., B.G., and B.W. thank the Center for Computationally Assisted Science and Technology (CCAST) at North Dakota State University and the National Energy Research Scientific Computing Center (NERSC) allocation awards 86678, supported by the Office of Science of the DOE under Contract No. DE-AC02-05CH11231. H.H. and S.K.D. acknowledge partial support from DOE BES FWP# LANLBES22. We also acknowledge the LANL Institutional Computing (IC) Program for providing computational resources.

REFERENCES

(1) Iijima, S. *Nature* **1991**, *354*, 56−58.
(2) Saito, R.; Dresselhaus, G.; Dresselhaus, M. S. *Physical Properties of Carbon Nanotubes*; Imperial College Press: London, 1998.
(3) Dass, D.; Prasher, R.; Vaid, R. *Int. J. Comput. Eng. Res.* **2012**, *2*, 1447−1457.
(4) Ando, T. *J. Phys. Soc. Jpn.* **2005**, *74*, 777−817.
(5) O'Connell, M. J.; Bachilo, S. M.; Huffman, C. B.; Moore, V. C.; Strano, M. S.; Haroz, E. H.; Rialon, K. L.; Boul, P. J.; Noon, W. H.; Kittrell, C.; et al. *Science* **2002**, *297*, 593−596.
(6) Sfeir, M. Y.; Beetz, T.; Wang, F.; Huang, L.; Huang, X. M. H.; Huang, M.; Hone, J.; O'Brien, S.; Misewich, J. A.; Heinz, T. F.; et al. *Science* **2006**, *312*, 554−556.
(7) Kataura, H.; Kumazawa, Y.; Maniwa, Y.; Umezu, I.; Suzuki, S.; Ohtsuka, Y.; Achiba, Y. *Synth. Met.* **1999**, *103*, 2555−2558.
(8) Brozena, A. H.; Kim, M.; Powell, L. R.; Wang, Y. *Nat. Rev. Chem.* **2019**, *3*, 375.
(9) He, X.; Hartmann, N. F.; Ma, X.; Kim, Y.; Ihly, R.; Blackburn, J. L.; Gao, W.; Kono, J.; Yomogida, Y.; Hirano, A.; et al. *Nat. Photonics* **2017**, *11*, 577−582.
(10) Kilina, S.; Ramirez, J.; Tretiak, S. *Nano Lett.* **2012**, *12*, 2306−2312.
(11) Ramirez, J.; Mayo, M. L.; Kilina, S.; Tretiak, S. *Chem. Phys.* **2013**, *413*, 89−101.
(12) Miyauchi, Y.; Iwamura, M.; Mouri, S.; Kawazoe, T.; Ohtsu, M.; Matsuda, K. *Nat. Photonics* **2013**, *7*, 715−719.
(13) Piao, Y.; Meany, B.; Powell, L. R.; Valley, N.; Kwon, H.; Schatz, G. C.; Wang, Y. *Nat. Chem.* **2013**, *5*, 840−845.
(14) Gifford, B. J.; Kilina, S.; Htoon, H.; Doorn, S. K.; Tretiak, S. *J. Phys. Chem. C* **2018**, *122*, 1828−1838.
(15) Strano, M. S.; Dyke, C. A.; Usrey, M. L.; Barone, P. W.; Allen, M. J.; Shan, H.; Kittrell, C.; Hauge, R. H.; Tour, J. M.; Smalley, R. E. *Science* **2003**, *301*, 1519−1522.
(16) Hartmann, N. F.; Yalcin, S. E.; Adamska, L.; Hároz, E. H.; Ma, X.; Tretiak, S.; Htoon, H.; Doorn, S. K. *Nanoscale* **2015**, *7*, 20521−20530.
(17) Shiraki, T.; Shiraishi, T.; Juhász, G.; Nakashima, N. *Sci. Rep.* **2016**, *6*, 28393.
(18) Hartmann, N. F.; Velizhanin, K. A.; Haroz, E. H.; Kim, M.; Ma, X.; Wang, Y.; Htoon, H.; Doorn, S. K. *ACS Nano* **2016**, *10*, 8355−8365.
(19) Kim, M.; Adamska, L.; Hartmann, N. F.; Kwon, H.; Liu, J.; Velizhanin, K. A.; Piao, Y.; Powell, L. R.; Meany, B.; Doorn, S. K.; et al. *J. Phys. Chem. C* **2016**, *120*, 11268−11276.
(20) Shiraki, T.; Uchimura, S.; Shiraishi, T.; Onitsuka, H.; Nakashima, N. *Chem. Commun.* **2017**, *53*, 12544−12547.
(21) He, X.; Gifford, B. J.; Hartmann, N. F.; Ihly, R.; Ma, X.; Kilina, S. V.; Luo, Y.; Shayan, K.; Strauf, S.; Blackburn, J. L.; et al. *ACS Nano* **2017**, *11*, 10785−10796.
(22) Gifford, B. J.; Sifain, A. E.; Htoon, H.; Doorn, S. K.; Kilina, S.; Tretiak, S. *J. Phys. Chem. Lett.* **2018**, *9*, 2460−2468.
(23) Saha, A.; Gifford, B. J.; He, X.; Ao, G.; Zheng, M.; Kataura, H.; Htoon, H.; Kilina, S.; Tretiak, S.; Doorn, S. K. *Nat. Chem.* **2018**, *10*, 1089−1095.
(24) Shiraishi, T.; Shiraki, T.; Nakashima, N. *Nanoscale* **2017**, *9*, 16900−16907.
(25) Kim, M.; Wu, X.; Ao, G.; He, X.; Kwon, H.; Hartmann, N. F.; Zheng, M.; Doorn, S. K.; Wang, Y. *Chem.* **2018**, *4*, 2180−2191.
(26) Ghosh, S.; Bachilo, S. M.; Simonette, R. A.; Beckingham, K. M.; Weisman, R. B. *Science* **2010**, *330*, 1656−1659.
(27) Ao, G.; Khripin, C. Y.; Zheng, M. *J. Am. Chem. Soc.* **2014**, *136*, 10383−10392.
(28) Kilina, S.; Tretiak, S. *Adv. Funct. Mater.* **2007**, *17*, 3405−3420.
(29) Sharma, A.; Gifford, B. J.; Kilina, S. *J. Phys. Chem. C* **2017**, *121*, 8601−8612.
(30) Humphrey, W.; Dalke, A.; Schulten, K. *J. Mol. Graphics* **1996**, *14*, 33−38.
(31) Kryjevski, A.; Gifford, B.; Kilina, S.; Kilin, D. *J. Chem. Phys.* **2016**, *145*, 154112.
(32) Kryjevski, A.; Mihaylov, D.; Gifford, B.; Kilin, D. *J. Chem. Phys.* **2017**, *147*, 034106.
(33) Erck, A.; Sapp, W.; Kilina, S.; Kilin, D. *J. Phys. Chem. C* **2016**, *120*, 23197−23206.
(34) Furche, F.; Ahlrichs, R. *J. Chem. Phys.* **2002**, *117*, 7433−7447.
(35) Frisch, M. J.; Trucks, G. W.; Schlegel, H. B.; Scuseria, G. E.; Robb, M. A.; Cheeseman, J. R.; Scalmani, G.; Barone, V.; Mennucci, B.; Petersson, G. A.; et al. *Gaussian 09*; Gaussian, Inc.: Wallingford, CT, 2009.
(36) Lee, C.; Yang, W.; Parr, R. G. *Phys. Rev. B: Condens. Matter Mater. Phys.* **1988**, *37*, 785−789.
(37) Hehre, W. J.; Stewart, R. F.; Pople, J. A. *J. Chem. Phys.* **1969**, *51*, 2657−2664.
(38) Yanai, T.; Tew, D. P.; Handy, N. C. *Chem. Phys. Lett.* **2004**, *393*, 51−57.
(39) Adamska, L.; Nazin, G. V.; Doorn, S. K.; Tretiak, S. *J. Phys. Chem. Lett.* **2015**, *6*, 3873−3879.
(40) Kwon, H.; Furmanchuk, A.; Kim, M.; Meany, B.; Guo, Y.; Schatz, G. C.; Wang, Y. *J. Am. Chem. Soc.* **2016**, *138*, 6878−6885.

DOI: 10.1021/acs.nanolett.9b02926
Nano Lett. 2019, 19, 8503−8509